High–order perturbation of surfaces algorithms for the simulation of localized surface plasmon resonances in graphene nanotubes

David P. Nicholls*, Xin Tong

Department of Mathematics, Statistics, and Computer Science, University of Illinois at Chicago, Chicago, IL 60607, United States of America

A B S T R A C T

The plasmonics of two–dimensional materials, such as graphene, has become an important field over the past decade. The active tunability of graphene via electrical gating or chemical doping has generated a great deal of excitement among engineers seeking sensing devices. Consequently there is significant demand for robust and highly accurate computational capabilities which can simulate such materials. The class of High–Order Perturbation of Surfaces methods have proven to be particularly appropriate for this purpose. In this contribution we describe our recent efforts to utilize both Dirichlet–Neumann Operators and Impedance–Impedance Operators in these schemes. In addition, we present detailed numerical results which not only validate our simulations using the Method of Manufactured Solutions, but we also describe Localized Surface Plasmon Resonances in graphene nanotubes enclosing rod–shaped dielectric materials.

© 2020 IMACS. Published by Elsevier B.V. All rights reserved.

1. Introduction

Graphene is a single layer of carbon atoms in a honeycomb lattice which was first isolated experimentally in 2004 [54] resulting in the 2010 Nobel Prize in Physics to Geim [22] and Novoselov [53]. Graphene's semimetallic character permits electrostatic biasing which allows one to tune its electrical properties, unlike the noble metals, which also support plasmons. Plasmons in graphene have been exploited for a wide range of applications, including optical modulators [36,60,63], photodetectors [20,21,32,35,25], metasurfaces [19,5,31], polarization control devices [4,64], and sensors [34,58,28]. For a complete discussion of graphene including modeling, device design, and particular applications, we refer the interested reader to the survey article of Bludov, Ferriera, Peres and Vasilevskiy [6] and the text of Goncalves and Peres [24].

All of the classical numerical algorithms have been utilized to simulate structures featuring two–dimensional materials numerically, for instance, Finite Difference Methods [62,33], Finite Element Methods [30,29], Discontinous Galerkin Methods [27], Spectral Element Methods [17], and Spectral Methods [26,13,7], but it can be argued [38,44] that such volumetric approaches are greatly disadvantaged with an unnecessarily large number of unknowns for the piecewise homogeneous problems we consider here. Interfacial methods based upon Integral Equations [14] are a natural alternative but these also face difficulties. One challenge is that an Integral Equation solver will return the scattering returns only for a specified geometric configuration. For instance, if the interface shape is changed then the solver must be run again. Another difficulty is the dense and non-symmetric positive definite systems of linear equations which must be inverted with each simulation.

---

* Corresponding author.
   E-mail addresses: davidn@uic.edu (D.P. Nicholls), xtong20@uic.edu (X. Tong).
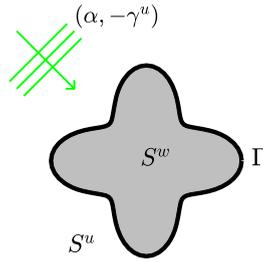
Fig. 1. Plot of the cross–section of a graphene nanotube, Γ, enclosing a material (occupying S^w) shaped by $r = \bar{g} + g(\theta) = \bar{g} + \varepsilon \cos(4\theta)$ ($\varepsilon = (3/10)\bar{g}$) housed in a dielectric (occupying S^u) under plane–wave illumination with wavenumber $(\alpha, -\gamma^u)$.

A "High Order Perturbation of Surfaces" (HOPS) approach [38,44] can effectively address these concerns. More specifically, we have in mind the method of Field Expansions (FE) which was introduced to generalize the low–order methods of Rayleigh [55] and Rice [56]. The high-order version of FE was first investigated by Bruno and Reitich [8–11], and later enhanced and stabilized by Nicholls and Reitich [48,49] resulting in the Method of Transformed Field Expansions (TFE). These algorithms maintain the advantageous properties of classical Integral Equation implementations (e.g., surface formulation and exact enforcement of far–field conditions) while avoiding the shortcomings stated above. For a description of the TFE approach to the bounded obstacle geometry see [43].

Our new approach is quite closely related to the work of Bruno and Reitich [11] who studied the same problem in the three–dimensional context of nanospheres. The current contribution differs in a number of ways beginning with its two–dimensional character (invariant in the third dimension) which requires the study of different Hankel functions. In addition we describe formulations in terms of either Dirichlet–Neumann Operators (DNOs) [37] or Impedance–Impedance Operators (IIOs) which permit the immediate simulation by other classical HOPS methods [8–11,49,43,50]. The IIO formulation is considered to avoid "Dirichlet eigenvalues" inherent to DNOs as advocated by Gillman, Barnett, and Martinsson [23].

The rest of the paper is organized as follows: In Section 2 we discuss the governing equations of our model for the response of a two–dimensional material mounted between two dielectrics. In Section 3 we outline our surface formulation of these equations in terms of both DNOs and IIOs. We present the conditions for a Localized Graphene Surface Plasmon Resonance (LGSPR) in this configuration in Section 4. In Section 5 we define the IIOs required for our surface formulation, and we discuss the FE (Section 5.1) and TFE methods (Section 5.2) for their computation. With this we describe our full HOPS methodology in Section 6. To conclude, we present our numerical results in Section 7 with a discussion of implementation issues in Section 7.1, validation by the Method of Manufactured Solutions in Section 7.2, and simulation of graphene nanotubes in Sections 7.3 and 7.4.

2. Governing equations

Following [51,52] the structure we consider is displayed in Fig. 1, a y–invariant nanotube of bounded cross–section with interface shaped by $r = \bar{g} + g(\theta)$. This interface separates two domains filled with materials of permittivities $\epsilon^{(u)}$ in $S^u := \{r > \bar{g} + g(\theta)\}$ and $\epsilon^{(w)}$ in $S^w := \{r < \bar{g} + g(\theta)\}$, respectively. The superscripts are chosen to conform to the notation of previous work by the authors [44,37,51,52]. The cylindrical geometry demands that the interface be 2π–periodic, $g(\theta + 2\pi) = g(\theta)$.

We consider monochromatic plane–wave illumination by incident radiation of frequency ω and wavenumber $k^u = n^u \omega / c_0 = \omega / c^u$ (c_0 is the speed of light), aligned with the corrugations of the obstacle. The scattered (electric or magnetic) fields are denoted by $\{u(r, \theta), w(r, \theta)\}$ in S^u and S^w, respectively, and the incident radiation in the outer domain by

$$u^{\text{inc}}(r, \theta) = e^{i\alpha x - i\gamma^u z} = e^{ir(\alpha \cos(\theta) - \gamma^u \sin(\theta))}.$$

The governing equations in this configuration are, for Transverse Electric (TE) and Transverse Magnetic (TM) polarization, [41,42]

$$\Delta u + (k^u)^2 u = 0, \qquad\qquad r > \bar{g} + g(\theta), \tag{2.1a}$$

$$\Delta w + (k^w)^2 w = 0, \qquad\qquad r < \bar{g} + g(\theta), \tag{2.1b}$$

$$u - w + A\tau^w \partial_N w = \xi, \qquad\qquad r = \bar{g} + g(\theta), \tag{2.1c}$$

$$\tau^u \partial_N u - \tau^w \partial_N w + Bw = \tau^u v, \qquad r = \bar{g} + g(\theta), \tag{2.1d}$$

$$\lim_{r \to \infty} r^{1/2} \left(\partial_r u - i k^u u \right) = 0, \tag{2.1e}$$

$$|w|_{L^\infty} < \infty, \qquad\qquad r < \bar{g} + g(\theta). \tag{2.1f}$$

where for $m \in \{u, w\}$

$$\tau^m = \begin{cases} 1, & \text{TE}, \\ 1/\epsilon^{(m)}, & \text{TM}, \end{cases} \qquad A = \begin{cases} 0, & \text{TE}, \\ \hat{\sigma}/(|N|\,(ik_0)), & \text{TM}, \end{cases} \qquad B = \begin{cases} |N|\,(ik_0)\hat{\sigma}, & \text{TE}, \\ 0, & \text{TM}, \end{cases}$$

and

$$\xi(\theta) := \left[-u^{\text{inc}} \right]_{r=\bar{g}+g(\theta)}, \quad v(\theta) := \left[-\partial_N u^{\text{inc}} \right]_{r=\bar{g}+g(\theta)}.$$

In these

$$\partial_N = \hat{r}(\bar{g}+g)\partial_r - \hat{\theta}\left(\frac{g'}{\bar{g}+g}\right)\partial_\theta,$$

for unit vectors in the radial ($\hat{r}$) and angular ($\hat{\theta}$) directions, while (2.1e) is the Sommerfeld radiation condition and (2.1f) expresses boundedness of solutions. Of particular note is $\hat{\sigma} = \sigma/(\epsilon_0 c_0)$, the dimensionless surface current which models the effects of the graphene deposited at the interface between the two layers [41,42].

3. Reformulation via surface integral operators

We now formulate (2.1) in terms of surface integral operators, first with Dirichlet–Neumann Operators (DNOs) and then with Impedance–Impedance Operators (IIOs). For the former we define the Dirichlet traces

$$U(x) := u(\bar{g}+g(\theta), \theta), \quad W(x) := w(\bar{g}+g(\theta), \theta),$$

and the outward pointing Neumann traces

$$\tilde{U}(x) := -(\partial_N u)(\bar{g}+g(\theta), \theta), \quad \tilde{W}(x) := (\partial_N w)(\bar{g}+g(\theta), \theta).$$

In terms of these, the boundary condition (2.1c) and (2.1d) read

$$U - W + A\tau^w \tilde{W} = \xi, \qquad\qquad r = \bar{g} + g(\theta), \tag{3.1a}$$
$$-\tau^u \tilde{U} - \tau^w \tilde{W} + BW = \tau^u v, \qquad r = \bar{g} + g(\theta). \tag{3.1b}$$

These specify two equations for four unknowns which would be problematic save that U and $\tilde{U}$ are connected, as are W and $\tilde{W}$. We formalize this with the following definition [51].

Definition 3.1. Given the unique outgoing solution to the Dirichlet problem

$$\Delta u + \left(k^u\right)^2 u = 0, \qquad\qquad r > \bar{g} + g(\theta), \tag{3.2a}$$
$$u(\bar{g}+g(\theta), \theta) = U(\theta), \tag{3.2b}$$
$$\lim_{r\to\infty} r^{1/2}\left(\partial_r u - ik^u u\right) = 0, \tag{3.2c}$$

the Neumann data, $\tilde{U}(\theta)$, can be computed. The DNO $G^{(u)}$ is defined by

$$G^{(u)}(g) : U \to \tilde{U}.$$

In addition we require the following definition.

Definition 3.2. If the bounded solution to the Dirichlet problem

$$\Delta w + \left(k^w\right)^2 w = 0, \qquad r < \bar{g} + g(\theta), \tag{3.3a}$$
$$w(\bar{g}+g(\theta), \theta) = W(\theta), \tag{3.3b}$$
$$|w|_{L^\infty} < \infty, \qquad\qquad r < \bar{g} + g(\theta), \tag{3.3c}$$

is unique, the Neumann data, $\tilde{W}(\theta)$, can be computed. The DNO $G^{(w)}$ is defined by

$$G^{(w)}(g) : W \to \tilde{W}.$$

In terms of these operators, (3.1) can now be written as [41,42]

$$
\begin{pmatrix} I & -I + A\tau^w G^{(w)} \\ \tau^w G^{(u)} & \tau^w G^{(w)} - B \end{pmatrix} \begin{pmatrix} U \\ W \end{pmatrix} = \begin{pmatrix} \xi \\ -\tau^u v \end{pmatrix}. \tag{3.4}
$$

Remark 3.3. As we explicitly accommodate in the definition, the possibility of non–unique solutions of the Dirichlet problem (3.3) exists. While this is not generic for a given configuration, it does inspire the IIO formulation given below.

Next, following [52], we formulate (2.1) in terms of IIOs. For this purpose we define the impedances

$$
I^{(u)} := \left[-\tau^u \partial_N u + Y u \right]_{r=\bar{g}+g}, \quad I^{(w)} := \left[\tau^w \partial_N w - Z w \right]_{r=\bar{g}+g},
$$

their "conjugates"

$$
\tilde{I}^{(u)} := \left[-\tau^u \partial_N u + Z u \right]_{r=\bar{g}+g}, \quad \tilde{I}^{(w)} := \left[\tau^w \partial_N w - Y w \right]_{r=\bar{g}+g},
$$

and the interfacial data

$$
\zeta := \left[-\tau^u v + Y \xi \right], \quad \psi := \left[-\tau^u v + Z \xi \right],
$$

where I is the identity, and Y and Z are unequal operators to be specified.

Remark 3.4. Before proceeding, we recall an analysis recently presented in [52] where we showed that the IIO problems (3.6) and (3.7) will each have a unique solution if the following conditions are met

$$
\mathrm{Im} \left\{ \int_{r=\bar{g}} \left(\left(\frac{Y}{\tau^u} \right) u \right) \bar{u} \, d\theta \right\} \leq 0, \quad \mathrm{Im} \left\{ \int_{r=\bar{g}} \left(\left(\frac{Z}{\tau^w} \right) w \right) \bar{w} \, d\theta \right\} \geq 0. \tag{3.5}
$$

Since $\tau^u \in \mathbf{R}^+$ the choice of Despres [15,16], $Y = -i\eta$ where $\eta \in \mathbf{R}^+$, satisfies (3.5). The situation with τ^w is more interesting as it can be complex. In particular, if $\epsilon^{(w)} = \epsilon^{(w)\prime} + i\epsilon^{(w)\prime\prime}$ and $Z = Z' + iZ''$, as

$$
\mathrm{Im} \left\{ \frac{Z}{\tau^w} \right\} = \begin{cases} Z'', & \text{TE,} \\ \epsilon^{(w)\prime} Z'', & \text{dielectric in TM,} \\ \epsilon^{(w)\prime} Z'' + \epsilon^{(w)\prime\prime} Z', & \text{metal in TM,} \end{cases}
$$

the Despres choice, $Z = i\eta$, satisfies (3.5) provided that the interior is not a metal ($\epsilon^{(w)\prime} < 0$ and $\epsilon^{(w)\prime\prime} > 0$) in TM polarization. In this case the choice of Z must be configuration specific, e.g.,

$$
\frac{Z''}{Z'} > \frac{-\epsilon^{(w)\prime}}{\epsilon^{(w)\prime\prime}} > 0,
$$

which can be accommodated.

We now give our two definitions.

Definition 3.5. Given an operator Y satisfying (3.5), the outgoing solution to

$$
\Delta u + \left(k^u \right)^2 u = 0, \qquad\qquad r > \bar{g} + g(\theta), \tag{3.6a}
$$

$$
-\tau^u \partial_N u(\bar{g} + g(\theta), \theta) + Y u(\bar{g} + g(\theta), \theta) = I^{(u)}(\theta), \tag{3.6b}
$$

$$
\lim_{r \to \infty} r^{1/2} \left(\partial_r u - ik^u u \right) = 0, \tag{3.6c}
$$

is unique and the impedance, $\tilde{I}^{(u)}(\theta)$, can be computed. The IIO Q is defined by

$$
Q(g) : I^{(u)} \to \tilde{I}^{(u)}.
$$

We also require the following definition.

Definition 3.6. Given an operator Z satisfying (3.5), the bounded solution to

$$\Delta w + \left(k^w\right)^2 w = 0, \qquad\qquad r < \bar{g} + g(\theta), \tag{3.7a}$$

$$\tau^w \partial_N w(\bar{g} + g(\theta), \theta) - Z w(\bar{g} + g(\theta), \theta) = I^{(w)}(\theta), \tag{3.7b}$$

$$|w|_{L^\infty} < \infty, \qquad\qquad r < \bar{g} + g(\theta), \tag{3.7c}$$

is unique and the impedance, $\tilde{I}^{(w)}(\theta)$, can be computed. The IIO S is defined by

$$S(g) : I^{(w)} \to \tilde{I}^{(w)}.$$

In terms of these, the boundary conditions (2.1c) and (2.1d) read

$$I^{(u)} + \tilde{I}^{(w)} + YA(I + Z(Y - Z)^{-1}(I - S))I^{(w)} - B(Y - Z)^{-1}(I - S)I^{(w)} = Y\xi - \tau^u \nu,$$

$$- \tau^u \tilde{I}^{(u)} - \tau^w \tilde{I}^{(w)} + ZA(I + Z(Y - Z)^{-1}(I - S))I^{(w)} - B(Y - Z)^{-1}(I - S)I^{(w)} = Z\xi - \tau^u \nu.$$

If we further assume that the operators Y and Z commute, then these equations can be written as

$$\begin{pmatrix} I & S + YA(Y - Z)^{-1}(Y - ZS) - B(Y - Z)^{-1}(I - S) \\ Q & I + ZA(Y - Z)^{-1}(Y - ZS) - B(Y - Z)^{-1}(I - S) \end{pmatrix} \begin{pmatrix} I^{(u)} \\ I^{(w)} \end{pmatrix} = \begin{pmatrix} \zeta \\ \psi \end{pmatrix}. \tag{3.9}$$

4. Localized graphene surface plasmon resonances

We are now in a position to search for the surface waves (the localized surface plasmons) which deliver field enhancements at the interface of the materials. For noble metals there is a classical formula to excite a Localized Surface Plasmon Resonance (LSPR) [18] and we seek an analogous condition here in the presence of graphene. Following [44] the condition for a Localized Graphene Surface Plasmon Resonance (LGSPR) is the singularity of the linearized operator (about the unperturbed, cylindrical, geometry) in the governing equations. More specifically, in terms of IIOs, for a TE LGSPR we would require that

$$M^{\mathrm{TE}} := \begin{pmatrix} I & S_0 - B_0(Y - Z)^{-1}(I - S_0) \\ Q_0 & I - B_0(Y - Z)^{-1}(I - S_0) \end{pmatrix}$$

be singular, and, for a TM LGSPR we would demand that

$$M^{\mathrm{TM}} := \begin{pmatrix} I & S_0 + YA_0(I + Z(Y - Z)^{-1}(I - S_0)) \\ Q_0 & I + ZA_0(I + Z(Y - Z)^{-1}(I - S_0)) \end{pmatrix}$$

be not invertible. At this point we follow Despres [15,16] and choose $Y = -Z = i\eta$ for a constant $\eta \in \mathbf{R}^+$. This leads us to consider singularities of the operators

$$M^{\mathrm{TE}} = \begin{pmatrix} I & S_0 - \frac{(ik_0)\hat{\sigma}}{2i\eta}(I - S_0) \\ Q_0 & I - \frac{(ik_0)\hat{\sigma}}{2i\eta}(I - S_0) \end{pmatrix},$$

and

$$M^{\mathrm{TM}} = \begin{pmatrix} I & S_0 + \frac{i\eta\hat{\sigma}}{2(ik_0)}(I + S_0) \\ Q_0 & I - \frac{i\eta\hat{\sigma}}{2(ik_0)}(I + S_0) \end{pmatrix}. \tag{4.1}$$

In [52] we observed that, for general Y and Z, solutions to (3.6) and (3.7) are given by

$$u(r, \theta) = \sum_{p=-\infty}^{\infty} \frac{(\widehat{I^{(u)}})_p}{-\tau^u(k^u \bar{g})H'_p(k^u \bar{g}) + \hat{Y}_p H_p(k^u \bar{g})} H_p(k^u r) e^{ip\theta},$$

$$w(r, \theta) = \sum_{p=-\infty}^{\infty} \frac{(\widehat{I^{(w)}})_p}{\tau^w(k^w \bar{g})J'_p(k^w \bar{g}) - \hat{Z}_p J_p(k^w \bar{g})} J_p(k^w r) e^{ip\theta},$$

where J_p is the p–th Bessel function and H_p is the p–th Hankel function of the first kind. From these we saw that

$$Q_0[I^{(u)}] = \sum_{p=-\infty}^{\infty} \left(\widehat{I^{(u)}}\right)_p \left(\frac{-\tau^u(k^u\bar{g})H_p'(k^u\bar{g}) + \hat{Z}_p H_p(k^u\bar{g})}{-\tau^u(k^u\bar{g})H_p'(k^u\bar{g}) + \hat{Y}_p H_p(k^u\bar{g})}\right) e^{ip\theta}, \tag{4.2a}$$

$$S_0[I^{(w)}] = \sum_{p=-\infty}^{\infty} \left(\widehat{I^{(w)}}\right)_p \left(\frac{\tau^w(k^w\bar{g})J_p'(k^w\bar{g}) - \hat{Y}_p J_p(k^w\bar{g})}{\tau^w(k^w\bar{g})J_p'(k^w\bar{g}) - \hat{Z}_p J_p(k^w\bar{g})}\right) e^{ip\theta}, \tag{4.2b}$$

which, upon setting $Y = -Z = i\eta$, define the order–one Fourier multipliers

$$Q_0 = \left(\frac{-\tau^u(k^u\bar{g})H_D'(k^u\bar{g}) - i\eta H_D(k^u\bar{g})}{-\tau^u(k^u\bar{g})H_D'(k^u\bar{g}) + i\eta H_D(k^u\bar{g})}\right), \quad S_0 = \left(\frac{\tau^w(k^w\bar{g})J_D'(k^w\bar{g}) - i\eta J_D(k^w\bar{g})}{\tau^w(k^w\bar{g})J_D'(k^w\bar{g}) + i\eta J_D(k^w\bar{g})}\right).$$

Thus, we can measure the singularity of M^{TE} and M^{TM} by examining the singularity of their actions at each wavenumber

$$\hat{M}_p^{\text{TE}} = \begin{pmatrix} 1 & (\widehat{S_0})_p - \frac{(ik_0)\hat{\sigma}}{2i\eta}\left[1 - (\widehat{S_0})_p\right] \\ (\widehat{Q_0})_p & 1 - \frac{(ik_0)\hat{\sigma}}{2i\eta}\left[1 - (\widehat{S_0})_p\right] \end{pmatrix},$$

and

$$\hat{M}_p^{\text{TM}} = \begin{pmatrix} 1 & (\widehat{S_0})_p + \frac{i\eta\hat{\sigma}}{2(ik_0)}\left[1 + (\widehat{S_0})_p\right] \\ (\widehat{Q_0})_p & 1 - \frac{i\eta\hat{\sigma}}{2(ik_0)}\left[1 + (\widehat{S_0})_p\right] \end{pmatrix},$$

which can, in turn, be characterized by a zero of the determinant functions

$$\tilde{\Delta}_p^{\text{TE}} = 1 - \frac{(ik_0)\hat{\sigma}}{2i\eta}\left[1 - (\widehat{S_0})_p\right] - (\widehat{Q_0})_p(\widehat{S_0})_p - \frac{(ik_0)\hat{\sigma}}{2i\eta}(\widehat{Q_0})_p\left[1 - (\widehat{S_0})_p\right], \tag{4.3a}$$

$$\tilde{\Delta}_p^{\text{TM}} = 1 - \frac{i\eta\hat{\sigma}}{2(ik_0)}\left[1 + (\widehat{S_0})_p\right] - (\widehat{Q_0})_p(\widehat{S_0})_p - \frac{i\eta\hat{\sigma}}{2(ik_0)}(\widehat{Q_0})_p\left[1 + (\widehat{S_0})_p\right]. \tag{4.3b}$$

With all of these considerations in hand we can investigate the possibility of exciting an LGSPR. However, there is one last piece of information that we require, namely the surface current model for the graphene. There are many models available for this purpose [24] and most are derived with a particular range of illumination frequencies, ω, in mind. In order to test multiple possibilities without overwhelming the reader, we have selected two models for our simulations. The first we found in the work of Angelis, Locatelli, Mutti, and Aceves [1,2] and it is an approximation due to Stauber, Peres and Neto [61] which accounts for both interband and intraband contributions. This "full" model is designed to be useful over a wide range of illumination frequencies but its form is rather opaque (see [6] for full details). By contrast, for lower frequencies, e.g. in the terahertz regime, the straightforward Drude model

$$\sigma_D = \sigma_0 \frac{4E_F}{\pi} \frac{1}{\hbar\gamma - i\hbar\omega},$$

is a simple and accurate model which is often employed [6], and so we use this as our second approximation.

With these models of graphene we now study the determinant functions (4.3) to examine the possibility of exciting an LGSPR. In order to eliminate the complicated frequency–dependent behavior of some popular dielectric materials, we consider a free–standing configuration where the inner and outer layers are filled with vacuum. We further investigate the effects of the size of the nanotube by considering two radii, $\bar{g} = 0.025$ microns and $\bar{g} = 1$ microns. Our results for the full model with $\bar{g} = 0.025$ microns are depicted in Fig. 2 for TE (left) and TM (right) polarization. These were repeated in the case $\bar{g} = 1$ microns and the output is shown in Fig. 3, again in TE (left) and TM (right) polarization. Each of these experiments was revisited with the Drude model for graphene, and the results are given for $\bar{g} = 0.025$ microns in Fig. 4, and for $\bar{g} = 1$ microns in Fig. 5. The inescapable conclusion is that an LGSPR can only be excited in TM polarization which matches the conclusion we reached in [51] in the absence of graphene.

5. Numerical simulation of the IIOs

Moving beyond this approximate formula to excite an LGSPR, $\tilde{\Delta}_p^{\text{TM}} \approx 0$ for some integer p, we investigate algorithms to simulate the full governing equations (3.9). For this, we now discuss how to compute the IIOs Q and S. In our previous work [52] we demonstrated the rigorous analyticity of these IIOs with respect to interface deformation for g sufficiently smooth (e.g., C^2 sufficed for our proof) and small. The proof begins with the assumption

$$g(\theta) = \varepsilon f(\theta), \quad f = \mathcal{O}(1), \quad \varepsilon \ll 1,$$

and explicitly justifies the expansions
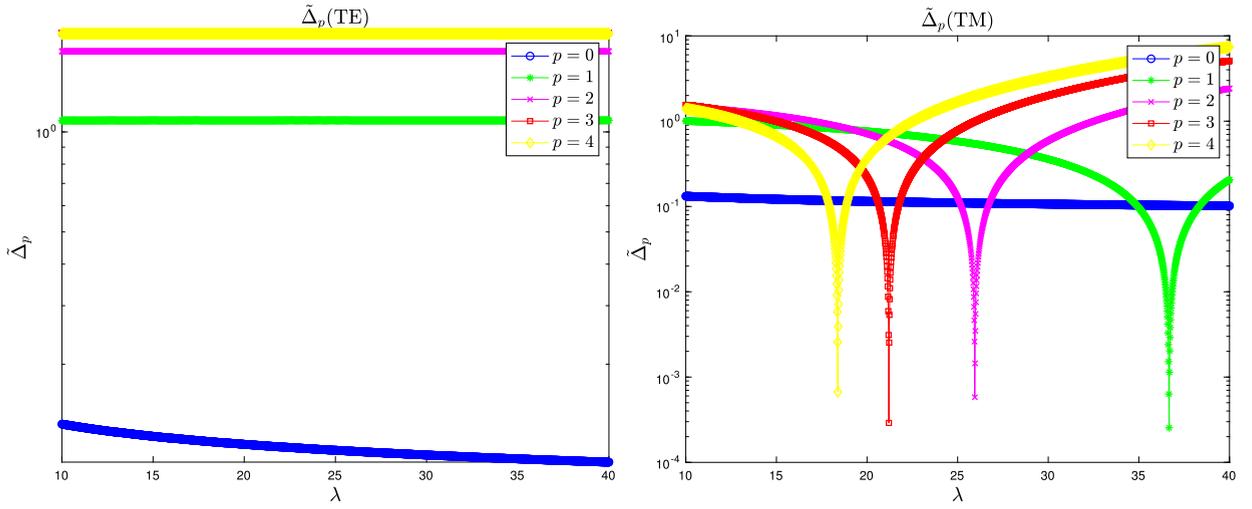
Fig. 2. Plot of the determinant function $\tilde{\Delta}_p$, (4.3), with the full model of graphene in (left) TE and (right) TM polarization for $\bar{g} = 0.025$ microns.
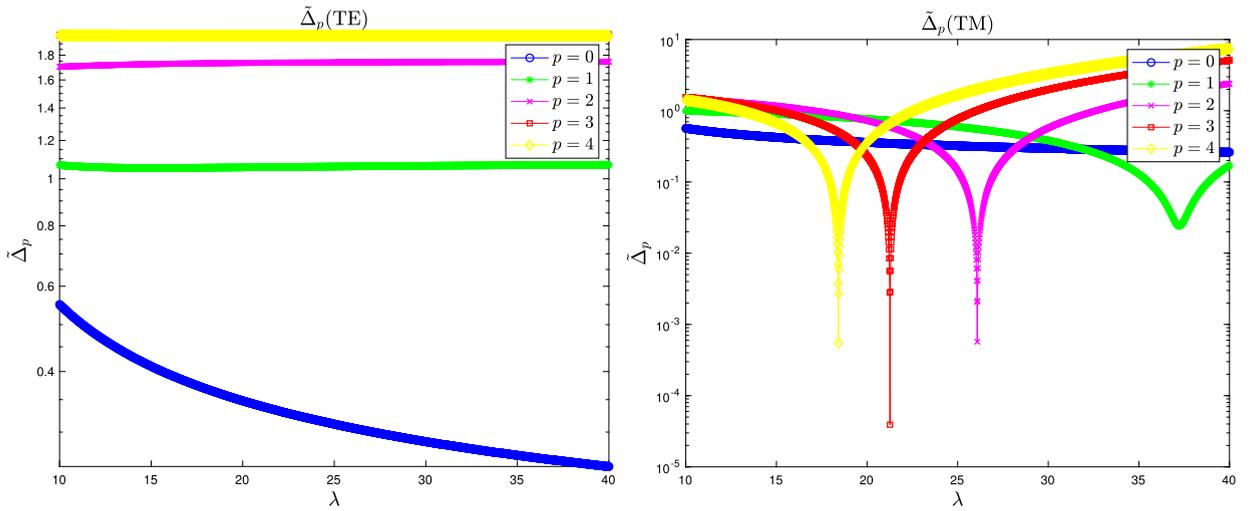
Fig. 3. Plot of the determinant function $\tilde{\Delta}_p$, (4.3), with the full model of graphene in (left) TE and (right) TM polarization for $\bar{g} = 1$ microns.
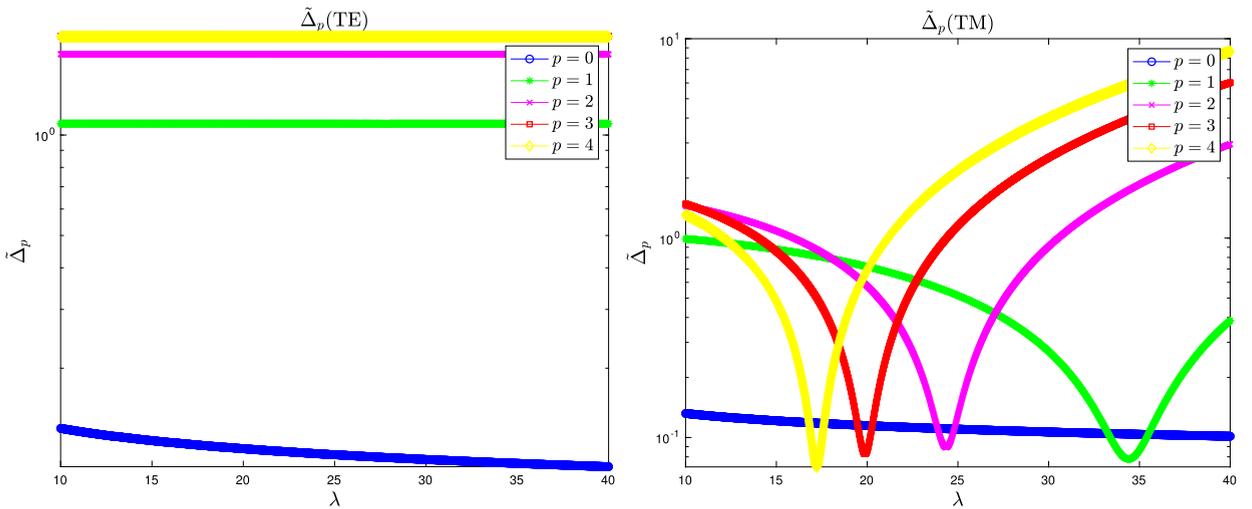
Fig. 4. Plot of the determinant function $\tilde{\Delta}_p$, (4.3), with the Drude model of graphene in (left) TE and (right) TM polarization for $\bar{g} = 0.025$ microns.
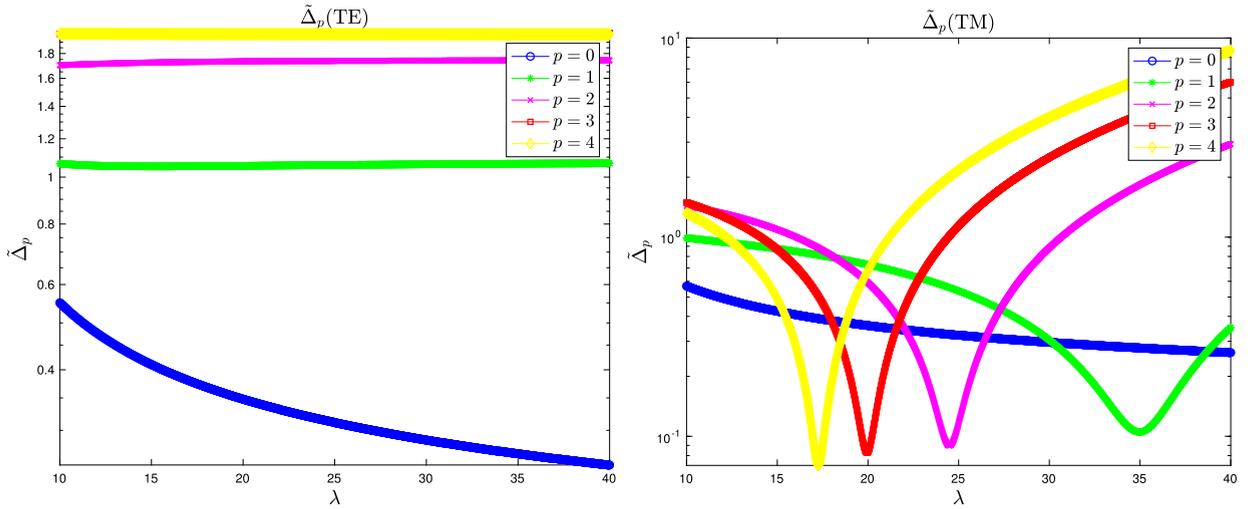
Fig. 5. Plot of the determinant function $\tilde{\Delta}_p$, (4.3), with the Drude model of graphene in (left) TE and (right) TM polarization for $\bar{g} = 1$ microns.

$$Q(\varepsilon f) = \sum_{n=0}^{\infty} Q_n(f)\varepsilon^n, \quad S(\varepsilon f) = \sum_{n=0}^{\infty} S_n(f)\varepsilon^n.$$

The question now becomes, can useful forms for the $\{Q_n, S_n\}$ be derived? We briefly describe two approaches here: The Method of Field Expansions (FE) due to Bruno and Reitich [8–10], and the Method of Transformed Field Expansions (TFE) devised by Nicholls and Reitich [45,49].

5.1. Field expansions

The FE approach begins with the supposition that the scattered fields also depend analytically upon ε (which is later verified). Focusing upon the field in the outer layer, $\{r > \bar{g} + g(\theta)\}$, this implies that

$$u = u(r, \theta; \varepsilon) = \sum_{n=0}^{\infty} u_n(r, \theta)\varepsilon^n.$$

Upon insertion of this into (3.6) one finds that the u_n must be outgoing solutions of the boundary value problem

$$\Delta u_n + (k^u)^2 u_n = 0, \qquad\qquad r > \bar{g}, \tag{5.1a}$$

$$-\tau^u \bar{g} \partial_r u_n + Y u_n = \delta_{n,0} I^{(u)} + L_n, \qquad r = \bar{g}, \tag{5.1b}$$

where $\delta_{n,m}$ is the Kronecker delta function, and

$$\begin{aligned}
L_n = &\frac{f}{\bar{g}}\delta_{n,1} I^{(u)} - Y \sum_{m=0}^{n-1} \partial_r^{n-m} u_m F_{n-m} - \frac{f}{\bar{g}} Y \sum_{m=0}^{n-1} \partial_r^{n-m-1} u_m F_{n-m-1} \\
&+ \tau^u \left[\bar{g} \sum_{m=0}^{n-1} \partial_r^{n-m+1} u_m F_{n-m} + 2f \sum_{m=0}^{n-1} \partial_r^{n-m} u_m F_{n-m-1} \right. \\
&\left. + \frac{f^2}{\bar{g}} \sum_{m=0}^{n-2} \partial_r^{n-m-1} u_m F_{n-m-2} - \frac{f'}{\bar{g}} \partial_\theta \sum_{m=0}^{n-1} \partial_r^{n-m-1} u_m F_{n-m-1} \right].
\end{aligned}$$

The outgoing solutions of (5.1a) are

$$u_n(r, \theta) = \sum_{p=-\infty}^{\infty} \hat{u}_{n,p} \frac{H_p(k^u r)}{H_p(k^u \bar{g})} e^{ip\theta},$$

and the $\hat{u}_{n,p}$ are determined recursively from the boundary conditions, (5.1b), beginning, at order zero, with

$$\hat{u}_{0,p} = \frac{\left(\widehat{I^{(u)}}\right)_p}{\left(-\tau^u \bar{g} \frac{H'_p(k^u \bar{g})}{H_p(k^u \bar{g})} + Y_p\right)}.$$

From this the IIO, Q, can be computed from

$$
\begin{aligned}
Q &= -\tau^u \partial_N u + Zu = \tau^u \left[-(\bar{g} + \varepsilon f)\partial_r u + \frac{\varepsilon f'}{\bar{g} + \varepsilon f}\partial_\theta u \right] + Zu \\
&= \sum_{n=0}^{\infty} \sum_{p=-\infty}^{\infty} \left\{ \tau^u \left[-k^u (\bar{g} + \varepsilon f)\frac{H'_p(k^u(\bar{g} + \varepsilon f))}{H_p(k^u \bar{g})} + \frac{\varepsilon f'}{(\bar{g} + \varepsilon f)}(ip)\frac{H_p(k^u(\bar{g} + \varepsilon f))}{H_p(k^u \bar{g})} \right] \right. \\
&\quad \left. + \hat{Z}_p \frac{H_p(k^u(\bar{g} + \varepsilon f))}{H_p(k^u \bar{g})} \right\} \hat{u}_{n,p} e^{ip\theta} \varepsilon^n.
\end{aligned}
$$

Expanding the Hankel functions $H_p(k^u(\bar{g} + \varepsilon f))$ and their derivatives in power series in ε, and equating like powers of ε we can find forms for the Q_n [51,52]. Similar considerations hold for the IIO S save that the alternate expansion

$$w_n(r,\theta) = \sum_{p=-\infty}^{\infty} \hat{w}_{n,p} \frac{J_p(k^w r)}{J_p(k^w \bar{g})} e^{ip\theta},$$

must be used.

5.2. Transformed field expansions

The TFE method proceeds in exactly the same manner as the FE approach above except that a "domain–regularizing" change of variables is affected before the expansion in ε is made. The change of variables essentially amounts to

$$r' = r - g(\theta), \quad \theta' = \theta,$$

which not only maps the deformed interface shape $\{r = \bar{g} + g(\theta)\}$ to the trivial shape $\{r = \bar{g}\}$, but also results in a greatly stabilized sequence of recursions. For complete details please see [52].

6. High–order perturbation of surfaces method

In light of the developments in the previous section regarding the computation of IIOs, we can now describe a rapid, highly accurate, and stable algorithm to compute solutions of the surface equations (3.9). In the interest of brevity we describe our approach for TM polarization ($B \equiv 0$) as the TE version ($A \equiv 0$) is quite similar.

To begin, we make Despres' choice [15,16] $Y = -Z = i\eta$, $\eta \in \mathbf{R}$, which simplifies (3.9) to

$$
\begin{pmatrix} |N| & |N| S + \left(\frac{i\eta}{2}\right)\left(\frac{\hat{\sigma}}{ik_0}\right)(I + S) \\ |N| Q & |N| - \left(\frac{i\eta}{2}\right)\left(\frac{\hat{\sigma}}{ik_0}\right)(I + S) \end{pmatrix} \begin{pmatrix} I^{(u)} \\ I^{(w)} \end{pmatrix} = \begin{pmatrix} |N| \zeta \\ |N| \psi \end{pmatrix}.
\tag{6.1}
$$

Again, making the HOPS assumption $g(\theta) = \varepsilon f(\theta)$, we suppose not only that the IIOs depend analytically upon ε but also that the surface fields do as well, so that

$$I^{(u)} = I^{(u)}(\theta; \varepsilon) = \sum_{n=0}^{\infty} I_n^{(u)}(\theta)\varepsilon^n, \quad I^{(w)} = I^{(w)}(\theta; \varepsilon) = \sum_{n=0}^{\infty} I_n^{(w)}(\theta)\varepsilon^n.$$

Upon insertion of these into (6.1), equating at like orders of ε delivers, at order zero,

$$
\begin{pmatrix} I & S_0 + \left(\frac{i\eta}{2}\right)\left(\frac{\hat{\sigma}}{ik_0}\right)(I + S_0) \\ Q_0 & I - \left(\frac{i\eta}{2}\right)\left(\frac{\hat{\sigma}}{ik_0}\right)(I + S_0) \end{pmatrix} \begin{pmatrix} I_0^{(u)} \\ I_0^{(w)} \end{pmatrix} = \begin{pmatrix} \zeta_0 \\ \psi_0 \end{pmatrix}.
\tag{6.2}
$$

At higher orders we find

$$
\begin{pmatrix} I & S_0 + \left(\frac{i\eta}{2}\right)\left(\frac{\hat{\sigma}}{ik_0}\right)(I + S_0) \\ Q_0 & I - \left(\frac{i\eta}{2}\right)\left(\frac{\hat{\sigma}}{ik_0}\right)(I + S_0) \end{pmatrix} \begin{pmatrix} I_n^{(u)} \\ I_n^{(w)} \end{pmatrix} = \begin{pmatrix} P_n \\ R_n \end{pmatrix},
\tag{6.3}
$$

where

$$P_n = \sum_{m=0}^{n} |N|_{n-m}\, \zeta_m - \sum_{m=0}^{n-1} |N|_{n-m}\, I_m^{(u)} - \sum_{m=0}^{n-1} S_{n-m} I_m^{(w)} - \left(\frac{i\eta}{2}\right)\left(\frac{\hat{\sigma}}{ik_0}\right) \sum_{m=0}^{n-1} S_{n-m} I_m^{(w)}$$

$$- \sum_{m=0}^{n-1} |N|_{n-m} \sum_{l=0}^{m} S_{m-l} I_l^{(w)},$$

$$R_n = \sum_{m=0}^{n} |N|_{n-m}\, \psi_m - \sum_{m=0}^{n-1} |N|_{n-m}\, I_m^{(u)} - \sum_{m=0}^{n-1} |N|_{n-m} \sum_{l=0}^{m} Q_{m-l} I_l^{(u)} - \sum_{m=0}^{n-1} |N|_{n-m}\, I_m^{(w)}$$

$$- \left(\frac{i\eta}{2}\right)\left(\frac{\hat{\sigma}}{ik_0}\right) \sum_{m=0}^{n-1} S_{n-m} I_m^{(w)},$$

and

$$|N| = |N|(\theta; \varepsilon) = \sum_{n=0}^{\infty} |N|_n(\theta)\varepsilon^n.$$

Appealing to our simple formulas for Q_0 and S_0, (4.2), and using the Fourier expansions

$$I_n^{(u)}(\theta) = \sum_{p=-\infty}^{\infty} \left(\widehat{I^{(u)}}\right)_{n,p} e^{ip\theta}, \quad I_n^{(w)}(\theta) = \sum_{p=-\infty}^{\infty} \left(\widehat{I^{(w)}}\right)_{n,p} e^{ip\theta},$$

we realize that (6.3) can be solved rapidly, as the only operator requiring inversion is (block 2×2) diagonalized by the Fourier transform.

7. Numerical results

We now present results of simulations using an implementation of the algorithm outlined above. The scheme is essentially a High–Order Spectral approach [26,13,17] with products approximated by convolutions implemented by the Fast Fourier Transform.

7.1. Implementation details

The numerical algorithm we analyze in this section utilizes the IIO formulation of the problem, (3.9), and the IIOs are simulated using the FE and TFE methods (see Section 5 and [51,52]). In order to approximate solutions of (6.1) we define

$$\left\{I^{(u)}, I^{(w)}\right\} \approx \left\{I_{N_\theta,N}^{(u)}, I_{N_\theta,N}^{(w)}\right\} := \sum_{n=0}^{N} \sum_{p=-N_\theta/2}^{N_\theta/2-1} \left\{\left(\widehat{I^{(u)}}\right)_{n,p}, \left(\widehat{I^{(w)}}\right)_{n,p}\right\} e^{ip\theta}\varepsilon^n.$$

An important consideration is how the series in ε are summed. For this, the classical numerical analytic continuation technique of Padé approximation [3] has been used very successfully for HOPS methods in the past (see, e.g., [9,47]) and we will use it here.

7.2. Validation by the method of manufactured solutions

Before proceeding to our numerical simulations, we validated our code using the Method of Manufactured Solutions (MMS) [12,57,59]. To summarize the MMS, when solving a system of partial differential equations subject to boundary conditions for an unknown, v, say

$$\mathcal{P}v = 0, \qquad \text{in } \Omega, \tag{7.1a}$$

$$\mathcal{B}v = 0, \qquad \text{at } \partial\Omega, \tag{7.1b}$$

it is typically just as easy to implement an algorithm to solve the "inhomogeneous" version of the above,

$$\mathcal{P}v = \mathcal{F}, \qquad \text{in } \Omega, \tag{7.2a}$$

$$\mathcal{B}v = \mathcal{J}, \qquad \text{at } \partial\Omega. \tag{7.2b}$$

In order to test an implementation, one begins with the "manufactured solution," $\tilde{v}$, and sets

$$\mathcal{F}_{\tilde{v}} := \mathcal{P}\tilde{v}, \quad \mathcal{J}_{\tilde{v}} := \mathcal{B}\tilde{v}.$$

Now, given this pair $\{\mathcal{F}_{\tilde{\nu}}, \mathcal{J}_{\tilde{\nu}}\}$ we have an *exact* solution to (7.2) against which we can compare our numerical simulation. While this provides no guarantee of a correct implementation, with a careful choice of $\tilde{\nu}$, e.g., one which displays the same qualitative behavior as solutions of (7.1), the approach can give great confidence in the accuracy of a scheme.

For the implementation in question we considered the 2π–periodic, outgoing solutions of the Helmholtz equation, (2.1a),

$$u^q(r, \theta) = A_u^q H_q(k^u r) e^{iq\theta}, \quad q \in \mathbf{Z}, \quad A_u^q \in \mathbf{C},$$

and the bounded counterpart for (2.1b)

$$w^q(r, \theta) = A_w^q J_q(k^w r) e^{iq\theta}, \quad q \in \mathbf{Z}, \quad A_w^q \in \mathbf{C}.$$

We selected an analytic profile

$$g(\theta) = \varepsilon f(\theta) = \varepsilon e^{\cos(\theta)}, \tag{7.3}$$

and defined, for a choice of the base radius of the interface $\bar{g}$, the Dirichlet and Neumann traces

$$u^{\text{exact}}(\theta) := u^q(\bar{g} + g(\theta), \theta), \quad \tilde{u}^{\text{exact}}(\theta) := (-\partial_N u^q)(\bar{g} + g(\theta), \theta),$$

and

$$w^{\text{exact}}(\theta) := w^q(\bar{g} + g(\theta), \theta), \quad \tilde{w}^{\text{exact}}(\theta) := (\partial_N w^q)(\bar{g} + g(\theta), \theta).$$

From these we computed the exact inner impedance

$$\tilde{I}^{(w),\text{exact}}(\theta) = \tau^w \tilde{w}^{\text{exact}} - i\eta w^{\text{exact}},$$

made the physical parameter choices

$$q = 2, \quad A_u^q = 2, \quad A_w^q = 1, \quad \eta = 3.4, \quad \lambda = 0.45, \tag{7.4a}$$

the numerical parameter choices

$$N_\theta = 64, \quad N_r = 32, \quad N = 16, \tag{7.4b}$$

and computed the approximation to $\tilde{I}^{(w),\text{exact}}$ by the FE and TFE algorithms delivering $\tilde{I}_{N_\theta,N}^{(w),\text{FE}}$ and $\tilde{I}_{N_\theta,N}^{(w),\text{TFE}}$, respectively. We point out that despite the fact that we chose $\eta > 0$, the algorithm delivered consistently accurate and stable results indicating that conditions (3.5) are sufficient but not necessary to ensure uniqueness of solutions. We measured the relative errors

$$\text{Error}_{\text{rel}}^{\text{FE}} = \frac{\left|\tilde{I}^{(w),\text{exact}} - \tilde{I}_{N_\theta,N}^{(w),\text{FE}}\right|_{L^\infty}}{\left|\tilde{I}^{(w),\text{exact}}\right|_{L^\infty}}, \quad \text{Error}_{\text{rel}}^{\text{TFE}} = \frac{\left|\tilde{I}^{(w),\text{exact}} - \tilde{I}_{N_\theta,N}^{(w),\text{TFE}}\right|_{L^\infty}}{\left|\tilde{I}^{(w),\text{exact}}\right|_{L^\infty}}, \tag{7.5}$$

and display our results in Fig. 6. From these we learn a number of important facts. First, from Fig. 6 (left), we see that if ε is sufficiently small (here $\varepsilon = \bar{g}/100$) then either HOPS approach (FE or TFE) with either summation mechanism (Taylor or Padé) will deliver excellent results (essentially machine precision) with a very *modest* choice of parameters. Here we see that with only 4–6 perturbation orders one fully resolves the exact MMS target, behavior that is consistent with that exhibited by HOPS schemes in other contexts [8,46,49,39].

However, as displayed in Fig. 6 (right), when the deformation size is large (here $\varepsilon = (2/5)\bar{g}$) the behavior of both the HOPS algorithms and the summation techniques diverges significantly. Here we see that the FE algorithm delivers excellent results through 8 perturbation orders, however, beyond this the Taylor summation algorithm produces divergent results while Padé approximants deliver consistent approximations. The TFE algorithm also produces robust simulations through 8 perturbation orders with a similar divergence of Taylor and Padé results at this point. As it has been not only proven [45,48,40] but also demonstrated numerically [46,49,39], the TFE approach produces *accurate* approximations of the Taylor coefficients in a *stable* fashion throughout *all* perturbation orders. Thus, we conclude that this value of ε is *outside* the disk of convergence of the relevant Taylor series. The fact that Padé summation of the TFE coefficients delivers the best results seen in Fig. 6 (right) indicates that not only does the domain of analyticity extend beyond this disk [47], but also that Padé summation is able to access this region of extended analyticity.

We repeated this convergence study with the more challenging profile

$$g(\theta) = \varepsilon f(\theta) = \varepsilon \cos(4\theta),$$

c.f., (7.8). Provided that we further refined the angular discretization to $N_\theta = 128$, we found results nearly identical to those depicted in Fig. 6.
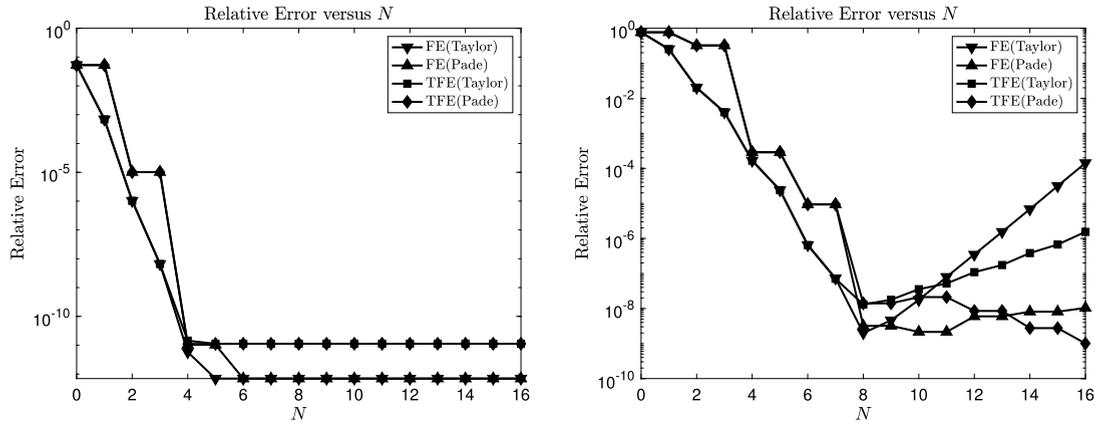
Fig. 6. Relative error (7.5) versus perturbation order for configuration (7.4) with (left) $\varepsilon = \bar{g}/100$ and (right) $\varepsilon = (2/5)\bar{g}$; FE and TFE schemes with Taylor and Padé summation.
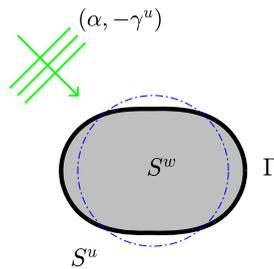
Fig. 7. Plot of the cross–section of a graphene nanotube, Γ, enclosing a material (occupying S^w) shaped by $r = \bar{g} + \varepsilon \cos(2\theta)$ ($\varepsilon = (1/5)\bar{g}$) housed in a dielectric (occupying S^u) under plane–wave illumination with wavenumber $(\alpha, -\gamma^u)$. The dash–dot blue line depicts the unperturbed geometry, the circle $r = \bar{g}$. (For interpretation of the colors in the figure(s), the reader is referred to the web version of this article.)

7.3. Graphene nanotubes with elliptically shaped cross–section

Having verified our code we proceeded to simulate bounded structures (nanorods) encased in graphene with cross–section shapes that are perturbations of a ring. A most natural such profile is given by

$$f(\theta) = \cos(2\theta), \tag{7.6}$$

which resembles an ellipse, see Fig. 7. Our experiments consisted of illuminating this structure over a range of N_λ–many incident wavelengths $\lambda_{\min} \leq \lambda \leq \lambda_{\max}$. For this initial simulation we considered the following physical parameters

$$\bar{g} = 0.025, 0.1, 1, \quad \lambda_{\min} = 35, \quad \lambda_{\max} = 40, \quad \varepsilon = \bar{g}/5. \tag{7.7a}$$

In addition, our FE algorithm required the following numerical discretization parameters

$$N_\lambda = 101, \quad N_\theta = 64, \quad N = 16. \tag{7.7b}$$

There are many outputs to this experiment that one could consider, each of which would indicate the presence or absence of an LGSPR. We chose to measure the L^2 norm of the output impedances, $\tilde{I}^{(u)}$ and $\tilde{I}^{(w)}$, which are produced as the outputs of the maps Q and S respectively. While these do not have obvious physical interpretations, they are readily computed Quantities of Interest (QoI) which will not only grow precipitously near an LGSPR, but also vary continuously as the interface shape is deformed by ε.

We began with the full model of graphene [61,1,2] and report our results in Fig. 8. Here we have plotted the QoI (the L^2 norms of Q (left column) and S (right column)) as $\bar{g}$ is varied among 0.025, 0.1, and 1 microns. From these figures we learn a number of things. First, regardless of the value of ε, there is a pronounced enhancement in the magnitude of the QoI at a particular value of λ indicating the excitation of an LGSPR. This enhancement is not only significant in magnitude but also quite sensitive in its response (its excitation range can be less than a nanometer). Beyond this, both the strength and sensitivity are significantly enhanced as the ring radius is decreased from 1 micron down to 0.025 microns. Finally, for all three radii, one sees a pronounced and easily identified shift in the LGSPR as the perfect ring is perturbed to an elliptically shaped one.
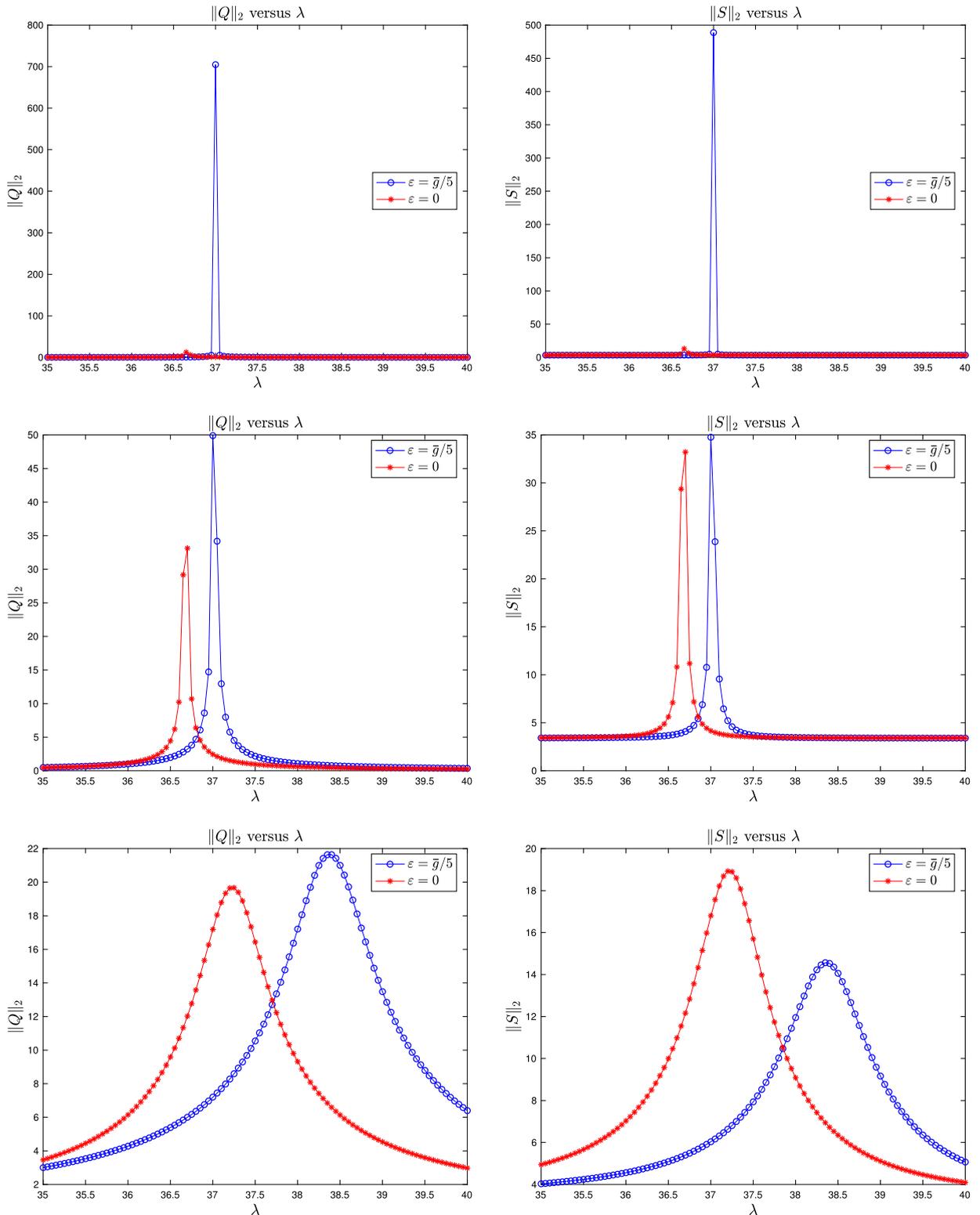
Fig. 8. Plot of the L^2 norms of Q (left column) and S (right column) for $\bar{g} = 0.025$ microns (top row), $\bar{g} = 0.1$ microns (middle row), and 1 micron (bottom row). The responses for a perfectly circular ring and the perturbed (elliptically shaped) ring are plotted in red and blue, respectively. The full model for graphene was utilized.

We repeated these experiments with the Drude model of graphene [6] and display our findings in Fig. 9. As before, we plotted the QoI (the L^2 norms of Q (left column) and S (right column)) as $\bar{g}$ is varied among 0.025 (top row), 0.1 (middle row), and 1 microns (bottom row). In order to properly observe all relevant effects we modified the range of λ in (7.7) to $\lambda_{\min} = 32$ and $\lambda_{\max} = 37$. The results here share similarities with our previous ones with the full graphene model. There is a decided enhancement regardless of ε and the range of wavelengths is still somewhat narrow. Also, there is still a shift as the interface shape is perturbed from circular to elliptical. However, it should be noted that each of these effects are significantly mollified in comparison to our results for the full graphene model. More specifically, the response range is much wider, the enhancement is not as pronounced, and the shift is much smaller when compared with the excitement spread in λ.

7.4. Graphene nanotubes with clover shaped cross–section

After studying graphene nanotubes with elliptically shaped cross–section we proceeded to consider clover shaped cross–sections of the form

$$f(\theta) = \cos(4\theta), \tag{7.8}$$

see Fig. 10. We conducted the same experiments as in the past section with the same parameters, (7.7), and our results for the full model of graphene are shown in Fig. 11. As in the case of the elliptically shaped graphene nanotube, there are several common features of these plots among all radii and perturbation sizes ε. First, an LGSPR is always excited which is indicated by an enhancement in the QoI (the L^2 norm of either Q or S). Furthermore, the response is always strong (though stronger for smaller radius $\bar{g}$) and quite narrow (though narrower for smaller $\bar{g}$). As above, in all cases there is a readily identified shift in the location of the LGSPR as a function of λ as the ring is deformed to a clover shape.

Our results for the Drude model of graphene are shown in Fig. 12. Once again, this classical model smears the rather "sharp" results for the full current model of graphene. However, there are, once again significant shifts in the LGSPR location for all configurations as the graphene geometry is deformed.

As we have seen, in every instance reported above, the location of the LGSPR changes as the shape of the cross–section of the graphene nanotube is deformed. We closed our investigations with a quantitative study of how this shift varied as the base radius was changed. The shift was defined as the (absolute value of) the difference in incident wavelength of the LGSPR for a perfectly circular cross–section ($\varepsilon = 0$) and the incident wavelength of the LGSPR excited by the perturbed geometry ($\varepsilon = \bar{g}/5$). We have plotted this shift versus base radius $\bar{g}$ in Fig. 13 over values

$$\bar{g} = 0.025, 0.05, 0.1, 0.2, 0.5, 1.$$

Here we see how the shift increases, essentially monotonically, as $\bar{g}$ is increased.

8. Conclusion

In this contribution we have taken up the questions of the existence and properties of Localized Graphene Surface Plasmon Resonances (LGSPRs). Using a generalization of our interfacial formulation of the problem of scattering of electromagnetic radiation by a nanorod (which accounts for the presence of graphene with a surface current), we were able to investigate these questions in a careful and rigorous fashion. Using two popular surface current models for graphene we gave evidence that LGSPRs can only be observed in Transverse Magnetic polarization akin to the same conclusion in the absence of this two–dimensional material. Beyond this we used a rapid, robust, and high–order accurate numerical scheme to investigate the effects of perturbing the shape of a perfectly cylindrical (circular cross–section) nanotube upon the appearance and characteristics of LGSPRs. We found these LGSPRs exist for any perturbation size, but that they can be significantly "moved," with quite modest shape deformation, in that they occur for values of incident illumination wavelength quite different than for the zero–deformation case. This interesting phenomena (also observed for periodic gratings) suggests a novel mechanism for sensing in the nanoscale regime.

Acknowledgements

References

[1] C.D. Angelis, A. Locatelli, A. Mutti, A. Aceves, Coupling dynamics of 1d surface plasmon polaritons in hybrid graphene systems, Opt. Lett. 41 (2016) 480–483.
[2] A. Auditore, C. de Angelis, A. Locatelli, A.B. Aceves, Tuning of surface plasmon polaritons beat length in graphene directional couplers, Opt. Lett. 38 (2013) 4228–4231.
[3] G.A. Baker Jr., P. Graves-Morris, Padé Approximants, second ed., Cambridge University Press, Cambridge, 1996.
[4] Q. Bao, H. Zhang, B. Wang, Z. Ni, C.H.Y.X. Lim, Y. Wang, D.Y. Tang, K.P. Loh, Broadband graphene polarizer, Nat. Photonics 5 (2011) 411–415.
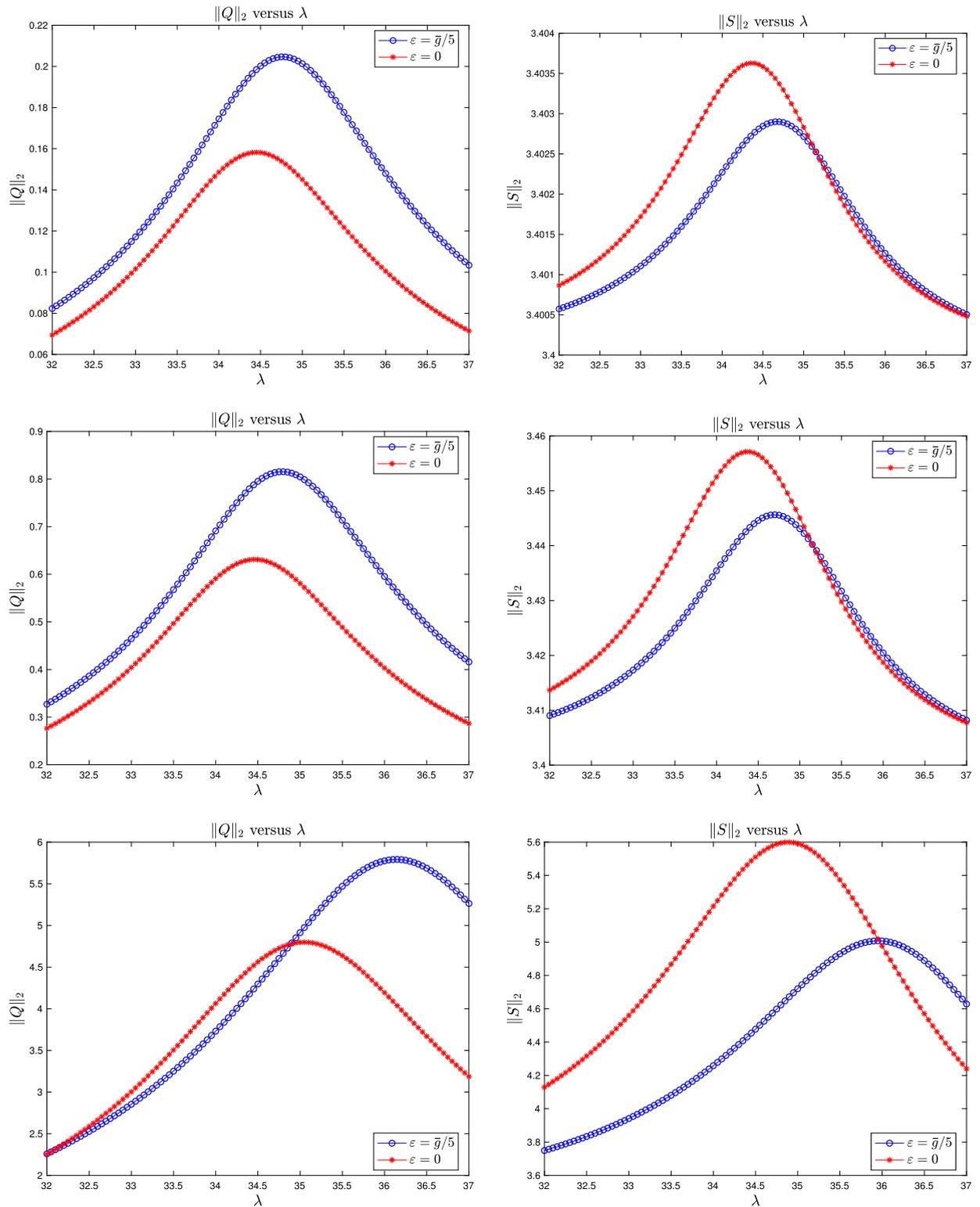
Fig. 9. Plot of the L^2 norms of Q (left column) and S (right column) for $\bar{g} = 0.025$ microns (top row), $\bar{g} = 0.1$ microns (middle row), and 1 micron (bottom row). The responses for a perfectly circular ring and the perturbed (elliptically shaped) ring are plotted in red and blue, respectively. The Drude model for graphene was utilized.
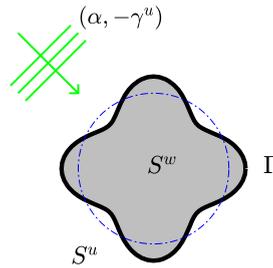
Fig. 10. Plot of the cross–section of a graphene nanotube, Γ, enclosing a material (occupying S^w) shaped by $r = \bar{g} + \varepsilon \cos(4\theta)$ ($\varepsilon = (1/5)\bar{g}$) housed in a dielectric (occupying S^u) under plane–wave illumination with wavenumber $(\alpha, -\gamma^u)$. The dash–dot blue line depicts the unperturbed geometry, the circle $r = \bar{g}$.

[5] S.R. Biswas, C.E. Gutiérrez, A. Nemilentsau, I.H. Lee, S.H. Oh, P. Avouris, T. Low, Tunable graphene metasurface reflectarray for cloaking, illusion, and focusing, Phys. Rev. Appl. 9 (2018) 034021.
[6] Y. Bludov, A. Ferreira, N. Peres, M. Vasilevskiy, A primer on surface plasmon–polaritons in graphene, Int. J. Mod. Phys. B 27 (2013) 1341001.
[7] J.P. Boyd, Chebyshev and Fourier Spectral Methods, second ed., Dover Publications Inc., Mineola, NY, 2001.
[8] O. Bruno, F. Reitich, Numerical solution of diffraction problems: a method of variation of boundaries, J. Opt. Soc. Am. A 10 (1993) 1168–1175.
[9] O. Bruno, F. Reitich, Numerical solution of diffraction problems: a method of variation of boundaries. II. Finitely conducting gratings, Padé approximants, and singularities, J. Opt. Soc. Am. A 10 (1993) 2307–2316.
[10] O. Bruno, F. Reitich, Numerical solution of diffraction problems: a method of variation of boundaries. III. Doubly periodic gratings, J. Opt. Soc. Am. A 10 (1993) 2551–2562.
[11] O.P. Bruno, F. Reitich, Boundary–variation solutions for bounded–obstacle scattering problems in three dimensions, J. Acoust. Soc. Am. 104 (1998) 2579–2583.
[12] O.R. Burggraf, Analytical and numerical studies of the structure of steady separated flows, J. Fluid Mech. 24 (1966) 113–151.
[13] C. Canuto, M.Y. Hussaini, A. Quarteroni, T.A. Zang, Spectral Methods in Fluid Dynamics, Springer-Verlag, New York, 1988.
[14] D. Colton, R. Kress, Inverse Acoustic and Electromagnetic Scattering Theory, second ed., Springer-Verlag, Berlin, 1998.
[15] B. Després, Méthodes de décomposition de domaine pour les problèmes de propagation d'ondes en régime harmonique. Le théorème de Borg pour l'équation de Hill vectorielle, Institut National de Recherche en Informatique et en Automatique (INRIA), Rocquencourt, 1991. Thèse, Université de Paris IX (Dauphine), Paris, 1991.
[16] B. Després, Domain decomposition method and the Helmholtz problem, in: Mathematical and Numerical Aspects of Wave Propagation Phenomena, Strasbourg, 1991, SIAM, Philadelphia, PA, 1991, pp. 44–52.
[17] M.O. Deville, P.F. Fischer, E.H. Mund, High-Order Methods for Incompressible Fluid Flow, Cambridge Monographs on Applied and Computational Mathematics, vol. 9, Cambridge University Press, Cambridge, 2002.
[18] S. Enoch, N. Bonod, Plasmonics: From Basics to Advanced Topics, Springer Series in Optical Sciences, Springer, New York, 2012.
[19] A. Fallahi, J. Perruisseau-Carrier, Design of tunable biperiodic graphene metasurfaces, Phys. Rev. B 86 (2012) 195408.
[20] Z. Fang, Z. Liu, Y. Wang, P.M. Ajayan, P. Nordlander, N.J. Halas, Graphene-antenna sandwich photodetector, Nano Lett. 12 (2012) 3808–3813.
[21] M. Freitag, T. Low, W. Zhu, H. Yan, F. Xia, P. Avouris, Photocurrent in graphene harnessed by tunable intrinsic plasmons, Nat. Commun. 4 (2013) 1951.
[22] A. Geim, Random walk to graphene (Nobel lecture), Angew. Chem., Int. Ed. 50 (2011) 6966–6985.
[23] A. Gillman, A. Barnett, P. Martinsson, A spectrally accurate direct solution technique for frequency-domain scattering problems with variable media, BIT Numer. Math. 55 (2015) 141–170.
[24] P.A.D. Goncalves, N.M.R. Peres, An Introduction to Graphene Plasmonics, World Scientific, Singapore, 2016.
[25] S. Goossens, G. Navickaite, C. Monasterio, S. Gupta, J.J. Piqueras, R.P. rez, G. Burwell, I. Nikitskiy, T. Lasanta, T. Galán, E. Puma, A. Centeno, A. Pesquera, A. Zurutuza, G. Konstantatos, F. Koppens, Broadband image sensor array based on graphene-cmos integration, Nat. Photonics 11 (2017) 366–371.
[26] D. Gottlieb, S.A. Orszag, Numerical Analysis of Spectral Methods: Theory and Applications, CBMS-NSF Regional Conference Series in Applied Mathematics, vol. 26, Society for Industrial and Applied Mathematics, Philadelphia, Pa, 1977.
[27] J.S. Hesthaven, T. Warburton, Nodal Discontinuous Galerkin Methods, Texts in Applied Mathematics, vol. 54, Springer, New York, 2008. Algorithms, analysis, and applications.
[28] H. Hu, X. Yang, F. Zhai, D. Hu, R. Liu, K. Liu, Z. Sun, Q. Dai, Far-field nanoscale infrared spectroscopy of vibrational fingerprints of molecules with graphene plasmons, Nat. Commun. 7 (2016) 12334.
[29] F. Ihlenburg, Finite Element Analysis of Acoustic Scattering, Springer-Verlag, New York, 1998.
[30] C. Johnson, Numerical Solution of Partial Differential Equations by the Finite Element Method, Cambridge University Press, Cambridge, 1987.
[31] L. Ju, B. Geng, J. Horng, C. Girit, M. Martin, Z. Hao, H.A. Bechtel, X. Liang, A. Zettl, Y.R. Shen, F. Wang, Graphene plasmonics for tunable terahertz metamaterials, Nat. Nanotechnol. 6 (2011) 630–634.
[32] F.H.L. Koppens, T. Mueller, P. Avouris, A.C. Ferrari, M.S. Vitiello, M. Polini, Photodetectors based on graphene, other two-dimensional materials and hybrid systems, Nat. Nanotechnol. 9 (2014) 780–793.
[33] R.J. LeVeque, Finite Difference Methods for Ordinary and Partial Differential Equations, Society for Industrial and Applied Mathematics (SIAM), Philadelphia, PA, 2007. Steady-state and time-dependent problems.
[34] Y. Li, H. Yan, D.B. Farmer, X.P. Meng, W. Zhu, R. Osgood, T.F. Heinz, P. Avouris, Graphene plasmon enhanced vibrational sensing of surface-adsorbed layers, Nano Lett. 14 (3) (2014) 1573–1577.
[35] C.-H. Liu, Y.-C. Chang, T.B. Norris, Z. Zhong, Graphene photodetectors with ultra-broadband and high responsivity at room temperature, Nat. Nanotechnol. 9 (2014) 273–278.
[36] M. Liu, X. Yin, E. Ulin-Avila, B. Geng, T. Zentgraf, L. Ju, F. Wang, X. Zhang, A graphene-based broadband optical modulator, Nature 474 (2011) 64–67.
[37] D.P. Nicholls, Three–dimensional acoustic scattering by layered media: a novel surface formulation with operator expansions implementation, Proc. R. Soc. Lond. A 468 (2012) 731–758.
[38] D.P. Nicholls, A method of field expansions for vector electromagnetic scattering by layered periodic crossed gratings, J. Opt. Soc. Am. A 32 (2015) 701–709.
[39] D.P. Nicholls, High–order perturbation of surfaces short course: boundary value problems, in: Lectures on the Theory of Water Waves, in: London Math. Soc. Lecture Note Ser., vol. 426, Cambridge Univ. Press, Cambridge, 2016, pp. 1–18.
[40] D.P. Nicholls, High–order perturbation of surfaces short course: analyticity theory, in: Lectures on the Theory of Water Waves, in: London Math. Soc. Lecture Note Ser., vol. 426, Cambridge Univ. Press, Cambridge, 2016, pp. 32–50.
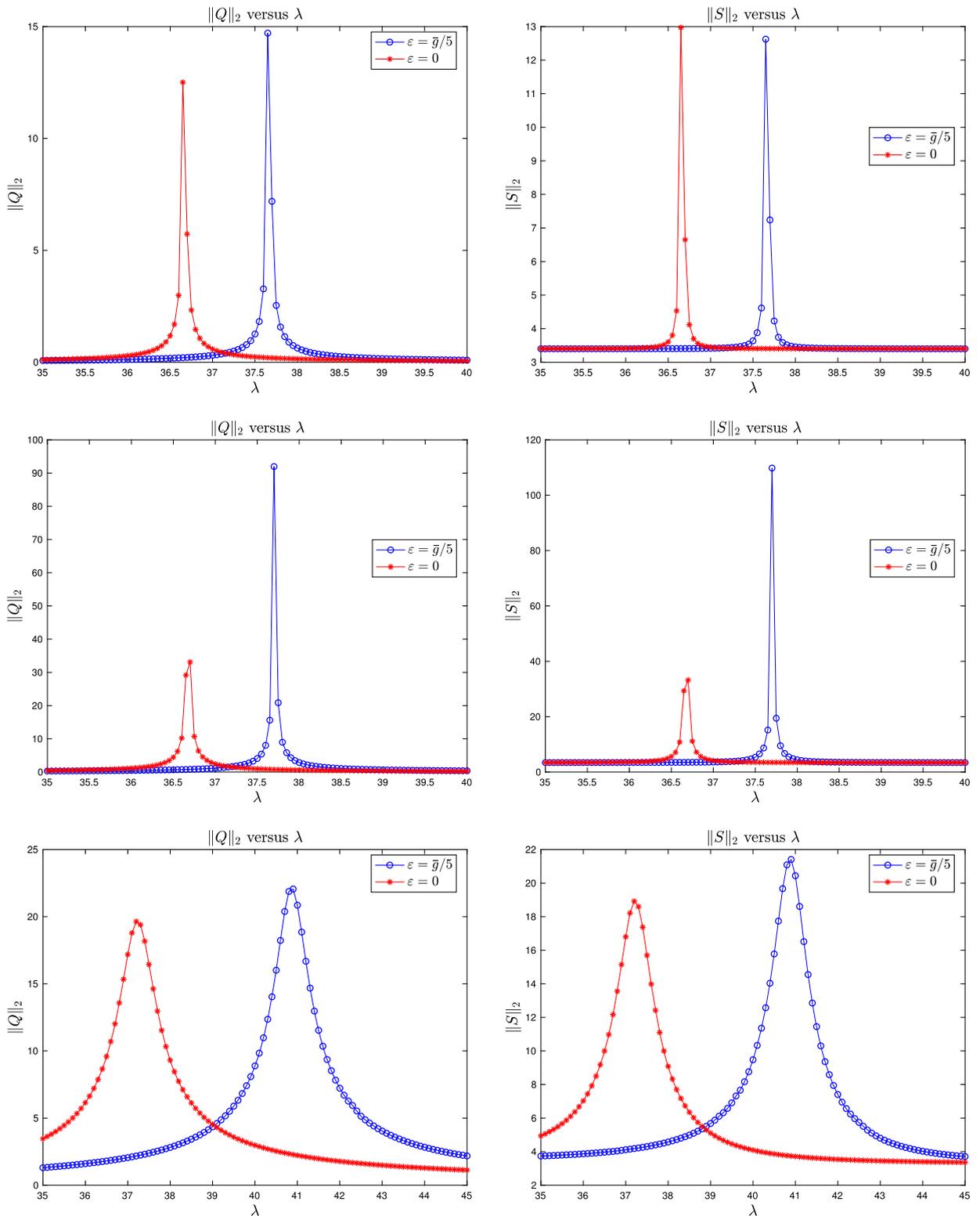
Fig. 11. Plot of the L^2 norms of Q (left column) and S (right column) for $\bar{g} = 0.025$ microns (top row), $\bar{g} = 0.1$ microns (middle row), and 1 micron (bottom row). The responses for a perfectly circular ring and the perturbed (clover shaped) ring are plotted in red and blue, respectively. The full model for graphene was utilized.
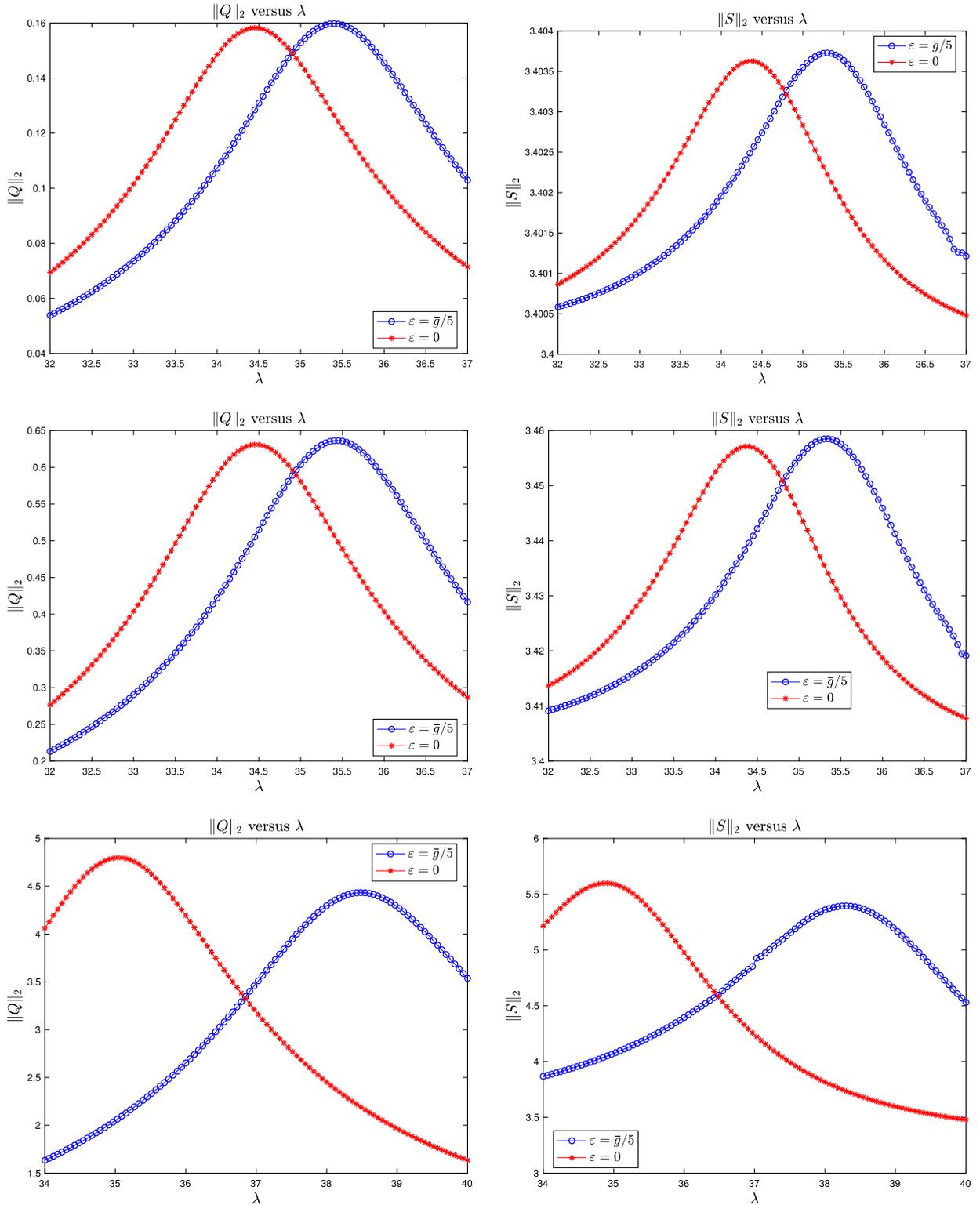
Fig. 12. Plot of the L^2 norms of Q (left column) and S (right column) for $\bar{g} = 0.025$ microns (top row), $\bar{g} = 0.1$ microns (middle row), and 1 micron (bottom row). The responses for a perfectly circular ring and the perturbed (clover shaped) ring are plotted in red and blue, respectively. The Drude model for graphene was utilized.
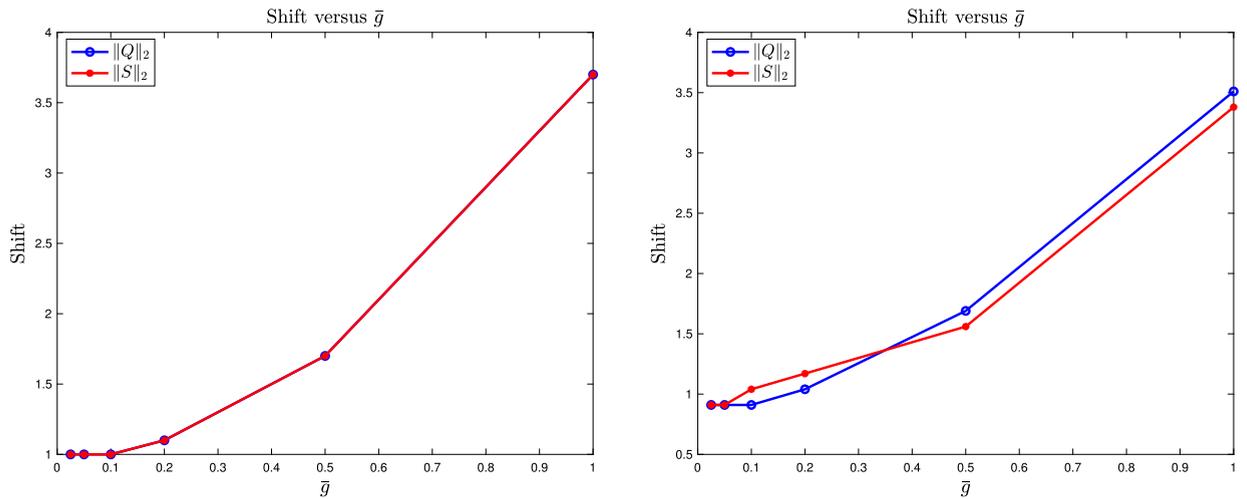
Fig. 13. Shift in excitation wavelength (in microns) of LGSPR as nanotube is deformed from $\varepsilon = 0$ to $\varepsilon = \bar{g}/5$ versus base radius, $\bar{g}$, for (a.) full model and (b.) Drude model of graphene.

[41] D.P. Nicholls, Numerical simulation of grating structures incorporating two–dimensional materials: a high–order perturbation of surfaces framework, SIAM J. Appl. Math. 78 (2018) 19–44.

[42] D.P. Nicholls, High–order spectral simulation of graphene ribbons, Commun. Comput. Phys. 26 (2019) 1575–1596.

[43] D.P. Nicholls, N. Nigam, Exact non-reflecting boundary conditions on general domains, J. Comput. Phys. 194 (2004) 278–303.

[44] D.P. Nicholls, S.-H. Oh, T.W. Johnson, F. Reitich, Launching surface plasmon waves via vanishingly small periodic gratings, J. Opt. Soc. Am. A 33 (2016) 276–285.

[45] D.P. Nicholls, F. Reitich, A new approach to analyticity of Dirichlet-Neumann operators, Proc. R. Soc. Edinb., Sect. A 131 (2001) 1411–1433.

[46] D.P. Nicholls, F. Reitich, Stability of high-order perturbative methods for the computation of Dirichlet-Neumann operators, J. Comput. Phys. 170 (2001) 276–298.

[47] D.P. Nicholls, F. Reitich, Analytic continuation of Dirichlet-Neumann operators, Numer. Math. 94 (2003) 107–146.

[48] D.P. Nicholls, F. Reitich, Shape deformations in rough surface scattering: cancellations, conditioning, and convergence, J. Opt. Soc. Am. A 21 (2004) 590–605.

[49] D.P. Nicholls, F. Reitich, Shape deformations in rough surface scattering: improved algorithms, J. Opt. Soc. Am. A 21 (2004) 606–621.

[50] D.P. Nicholls, J. Shen, A stable, high-order method for two–dimensional bounded–obstacle scattering, SIAM J. Sci. Comput. 28 (2006) 1398–1419.

[51] D.P. Nicholls, X. Tong, A high–order perturbation of surfaces algorithm for the simulation of localized surface plasmon resonances in two dimensions, J. Sci. Comput. 76 (2018) 1370–1395.

[52] D.P. Nicholls, X. Tong, Simulation of localized surface plasmon resonances in two dimensions via impedance–impedance operators, SIAM J. Appl. Math. (2019), submitted for publication.

[53] K. Novoselov, Graphene: materials in the flatland (Nobel lecture), Angew. Chem., Int. Ed. 50 (2011) 6986–7002.

[54] K.S. Novoselov, A.K. Geim, S.V. Morozov, D. Jiang, Y. Zhang, S.V. Dubonos, I.V. Grigorieva, A.A. Firsov, Electric field effect in atomically thin carbon films, Science 306 (2004) 666–669.

[55] L. Rayleigh, On the dynamical theory of gratings, Proc. R. Soc. Lond. A 79 (1907) 399–416.

[56] S.O. Rice, Reflection of electromagnetic waves from slightly rough surfaces, Commun. Pure Appl. Math. 4 (1951) 351–378.

[57] P.J. Roache, Code verification by the method of manufactured solutions, J. Fluids Eng. 124 (2002) 4–10.

[58] D. Rodrigo, O. Limaj, D. Janner, D. Etezadi, F.J. García de Abajo, V. Pruneri, H. Altug, Mid-infrared plasmonic biosensing with graphene, Science 349 (2015) 165–168.

[59] C.J. Roy, Review of code and solution verification procedures for computational simulation, J. Comput. Phys. 205 (2005) 131–156.

[60] B. Sensale-Rodriguez, R. Yan, M.M. Kelly, T. Fang, K. Tahy, W.S. Hwang, D. Jena, L. Liu, H.G. Xing, Broadband graphene terahertz modulators enabled by intraband transitions, Nat. Commun. 3 (2012) 780.

[61] T. Stauber, N.M.R. Peres, A.H. Castro Neto, Conductivity of suspended and non-suspended graphene at finite gate voltage, Phys. Rev. B 78 (2008) 085418.

[62] J.C. Strikwerda, Finite Difference Schemes and Partial Differential Equations, second ed., Society for Industrial and Applied Mathematics (SIAM), Philadelphia, PA, 2004.

[63] Z. Sun, A. Martinez, F. Wang, Optical modulators with 2d layered materials, Nat. Photonics 10 (2016) 227–238.

[64] M. Tymchenko, A. Nikitin, L. Martín-Moreno, Faraday rotation due to excitation of magnetoplasmons in graphene microribbons, ACS Nano 7 (2013) 9780–9787.